Regular Paper

Aerial Photography Planning Method for 3D Model Creation to Realize Remote Inspection for Utility Poles

Koji Yamagishi*, Yuichi Tokunaga*

*Graduate School of Engineering, Kanazawa Institute of Technology, Japan
{c6301756@st, y.tokunaga@neptune}.kanazawa-it.ac.jp

Abstract - In this paper, we propose and verify a method for efficiently generating flight paths for aerial photography using drones, with the aim of reducing the labor required for inspecting utility poles in Japan. Utility poles are critical infrastructure supporting power and telecommunications networks; however, due to their large number and wide distribution, they are currently inspected manually. To carry out 3D model inspections for utility poles using drones, which are used for bridges and dams, it is necessary to plan the flight path and aerial photography points so that many utility poles can be photographed efficiently in a single flight.

Therefore, we devised an algorithm that aims to pass through the theoretically optimal photography position of the utility pole and searches for the optimal photography point on the main flight route while prioritizing constant-speed flight, thereby improving the model generation accuracy. Through computer evaluation, we confirmed that, compared to previous studies that assumed multirotor drones, the model accuracy of VTOL drones and this algorithm is equivalent, but flight time can be reduced by 72.6%.

Keywords: 3D model, Drone, Utility pole, Structure from Motion, Maintenance

1 INTRODUCTION

In recent years, several social infrastructure facilities have waged over 50 years since their construction, and the useful life of equipment is also considered to be 50 years [1].

For example, the United States has been developing infrastructure on a large scale since the New Deal policies in the 1930s [2]. Fifty years later, in the 1980s, the U.S. faced the fundamental problem of aging infrastructure that impacted various aspects of the economy and daily life [3]. Japan's social infrastructure was constructed intensively during rapid economic growth between 1955 and 1970. Fifty years later, Japan already has many aging facilities, and this number is expected to increase at an accelerating rate [4].

Maintenance of these facilities, including inspection and repair, is essential. Inspection is the task of evaluating the condition of equipment, and with inspection comes the process of selecting equipment to be repaired. The efficiency and accuracy of this process has a significant impact on overall maintenance. Several efficient inspection methods have been developed for use in various facilities. However, few studies have focused on inspection methods for utility poles, which are small structures. Utility poles are more numerous in larger facilities. The total number of utility poles in 2016 was 35.78 million and increased by approximately 70,000 per year. Of these, 67% are electric poles for power transmission and 33% are telegraph poles for telecommunications. Time, cost, and human efficiency must be emphasized when inspecting all utility poles.

Conventionally, utility pole inspections have relied on visual inspection characterized by high reliability and accuracy. However, visual inspections require inspectors to visit all utility poles on site, which is challenging because geographical factors and the height of the poles make it difficult to assess their condition. Consequently, visually inspecting all utility poles is inefficient in terms of time, money, and workforce.

Inspection methods that use three-dimensional (3D) models are being considered for large facilities. Tion et al. described a 3D reconstruction method for multi-vision-based inspection of pipelines [5]. They also presented an efficient and accurate 3D reconstruction method for industrial pipeline inspections using photogrammetry. The five photogrammetric methods used in this study were stereovision, photometric stereo, CAD-based photogrammetry, motion-based photogrammetry, and shading-based photogrammetry.

In addition, drones are used to acquire data for 3D model generation. Miyake et al. used a drone to capture aerial shots of a road's slope, fill, and a bridge to create a 3D model representing structures, slopes, and fills on the road [6]. This allowed identifying signs based on the differences between the current and past 3D models.

There are other reasons why labor-saving needs to be achieved. The number of construction workers, including infrastructure inspectors, has been decreasing since 1997, with 5 million in 2015, which is 73% of the peak; this shortage is expected to continue [7]. Therefore, as with large facilities, drones and 3D models are expected to be utilized; however, as mentioned earlier, utility poles need to be made more efficient in terms of their number.

Therefore, this study examines a method for generating high-precision 3D models of utility poles using aerial images captured by drones to improve the efficiency. Creating a 3D model of an entire utility pole using aerial photography with a drone allows inspections to be conducted remotely. As a result, inspections without relying on manpower become possible, and the efficiency improves.

On the other hand, the use of VTOL drones is being considered for wide-area inspections [8]. A VTOL drone can take off and land vertically like a helicopter and can cruise at high speeds, such as a fixed-wing aircraft. It can take off and land in confined spaces and is characterized by its ability to

travel long distances at high speeds [9]. Compared to a normal multirotor drone, a VTOL drone cannot perform maneuvers, such as hovering or turning. However, because they are able to travel long distances at high speeds, they can inspect a wide area within a short time.

Therefore, in this study, we propose an aerial photography point and a movement path generation algorithm suitable for VTOL drones. The contributions to this paper are summarized as follows:

- VTOL drones have the advantage of being more efficient with their batteries, as they have a longer range than multirotor drones; however, they also have the drawback of not being able to make sharp turns. By overcoming this disadvantage with the proposed algorithm, we were able to gain prospects for using VTOL drones to inspect the utility poles.

Section 2 introduces 3D models and related studies on their use and generation using aerial photography. Section 3 describes the proposed framework based on the hypotheses derived from these studies, and Section 4 describes the evaluation. Finally, conclusions are presented in Section 5.

2 RELATED WORK

In this section, previous drone 3D model generation methods are presented, and the requirements for 3D modeling of utility poles are clarified.

A 3D model comprises point-cloud data obtained using laser scanning or photogrammetry. Laser scanning is generally performed using LiDAR and 3D laser scanners. The time-of-flight method, which measures the time of travel due to laser emission and reflection, is used to obtain the spatial coordinates of an object's surface. Therefore, spatial coordinates can be accurately measured within an error range of 1–10 mm [10]. However, laser scanners are expensive, and their use may be limited by certain circumstances that can distort measurements, such as laser penetration and diffuse reflection.

The photogrammetric method acquires point-cloud data by reconstructing 2D images with overlapping intervals into a 3D point cloud. Point-cloud data are acquired using techniques such as Structure from Motion (SfM) and Multiview Stereo (MVS). SfM obtains spatial coordinates by superimposing multiple photos and calculating distances based on critical points in the photos. MVS refers to the recovery of a 3D shape from a camera's captured point. Photogrammetry methods are challenging because of their low accuracy.

However, photogrammetric methods are attracting attention as alternatives to LiDAR because of their low cost and ease of acquiring point clouds [11]. Therefore, various mobility-based imaging methods are being considered to efficiently acquire data in terms of time, money, and manpower.

Drones and other uncrewed aircraft are used for data acquisition. Yoon et al. proposed an unmanned aerial vehicle-based missing area detection and damage location method based on 3D image coordinates as an alternative to the visual inspection of piers [12]. Sungsik's methodology comprises the following three phases. In Phase 1, coordinate transformation is performed using the point and attitude information of the uncrewed aircraft and camera, and the distance information between the camera and the target surface is used to obtain the coordinates of the center point of each acquired image. In Phase 2, the focal length and working distance of the camera were used to calculate the field-of-view size for each acquired image. In Phase 3, information regarding the size of the field of view of all images computed in the previous phases was used to identify missing portions of the region of interest. This makes it possible to locate the damage detected at the individual image level in the entire inspection area.

The results showed that the missing areas and damaged locations could be identified with an error of 10 cm while leveraging the efficiency of uncrewed aerial vehicles. However, because utility poles are small-scale facilities, the 10-cm error becomes significant and cannot be ignored. Eliminating this error is necessary to generate a high-quality 3D model.

Moritani et al. proposed a method for estimating camera points for additional photography based on the results of low-quality region extraction as a guideline for optimal photography planning for efficient and high-quality 3D model generation using SfM-MVS [13]. This study focused on the fact that it is currently necessary to determine in advance the number of captured images from a location to generate a high-quality 3D model. In addition, if too many images are captured, the MVS process requires a significant amount of time. A related study used the procedure shown in Fig. 1 to predict the quality of a high-density model generated by the MVS process. The prediction relies solely on 3D tie points and camera poses estimated by the SfM process, which can be computed quickly. The study also estimated the optimal additional image capture points to improve the quality of regions predicted to be of low quality. The goal is to estimate the optimal additional image-capturing locations that can improve the quality of the predicted regions.

The specific procedure is to calculate additional candidate photography points where orthographic imaging of the low-quality area is possible from the center of gravity point of the low-quality area and then obtain an index of candidate

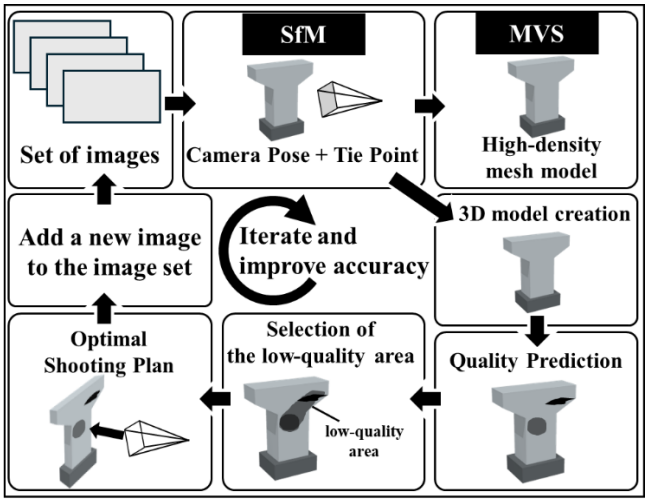

Figure 1: SfM-MVS process and proposed process.

additional photography points. The relationship between the calculated candidate additional photography points and the photography points that best covered the low-quality area among the already captured cameras was expressed as a particular index. The two indices were weighed and combined. This procedure was performed for all the candidates' additional photography points, and the additional photography points corresponding to the index with the lowest value were selected as the optimal point. Repeating this method allows for the efficient determination of additional photography points.

We compared the accuracy of the 3D model with three groups of images: 30 randomly selected images, 72 randomly selected images, and 72 images selected using the proposed method, from a set of 171 original images captured densely around the outer circumference of the piers. The average error of the 30 randomly selected images was 12.3 mm, and that of the 72 selected images was 6.1 mm. By contrast, the proposed method with 72 images resulted in an error of 2.2 mm, indicating its effectiveness method for 3D model accuracy. However, although high accuracy can be obtained, the number of shots is large, and should be reduced while maintaining the accuracy of the 3D model.

Yamazaki et al. proposed an optimal acquisition planning method for 3D reconstruction using SfM/MVS for construction sites [14]. This study used the "model-based methods" method, a simple 3D model based on geospatial information to plan optimal photography locations and routes [15]. The specific process was to homogenize the simplified model by meshing. Next, from the candidate voxels for photography points, points that minimized the number of shots required for modeling were extracted. Minimizing the number of shots required to capture all the meshes reduces the cost of photography.

Consequently, the number of photography points was reduced from 1,790 to 83 for the target building. However, time efficiency was not considered when multiple photography points were far apart, and operational issues remained because the path setting was not considered.

If we focus on the type of drone, Yoon et al. used a drone that included a VTOL model. In contrast, the others assumed a low-efficiency multirotor drone, so they were unable to pursue true efficiency in terms of photography time.

In this study, we discuss an aerial photography route for utility poles that achieves both efficiency and accuracy, using the multirotor drones or VTOL drones introduced in Chapter 2. Specifically, we determined the aerial photography course while taking supplementary shots based on the photography point that minimizes the number of shots. When the photography points are discrete, additional points are estimated, and supplementary images are captured to ensure that the accuracy of the 3D model is not compromised.

3 PROPOSAL OF THE FRAMEWORK

3.1 Proposal Summary

This study created a flight path plan based on the optimal aerial photography point that minimized the number of cameras required to achieve both accuracy and time efficiency.

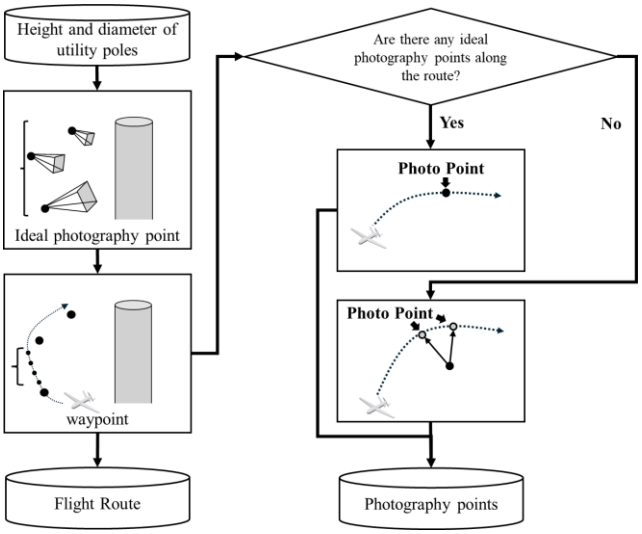

Figure 2: Proposal processing flow.

Furthermore, a path was created to perform drone aerial photography without compromising the temporal efficiency, allowing continuous flight at a constant speed. We followed this route and applied the complementary photography point-candidate extraction method described by Moritani et al. We performed interpolated photography to capture aerial shots without degrading the accuracy of the 3D model by capturing the images necessary for 3D model generation. The goal was to find the path with the shortest total aerial photography time using multiple aerial photography locations. Figure 2 shows the processing flow of the proposed method. The location data of the utility poles is used until the ideal photography point is calculated, and the information of the drone is added to calculate the waypoint. Based on the above, a flight route for generating a 3D model of a utility pole was calculated.

3.2 Flight Route Planning

The target was subdivided into smaller areas using a square mesh according to the method described by Yamazaki et al. The coordinates at which square meshes could be obtained simultaneously were determined. This can be expressed as a mathematical formula to optimize such that the binary variable x in Equation (1) is minimized. The index i represents the coordinates and orientation of a candidate photography viewpoint, while the corresponding variable x_i indicates whether this viewpoint is selected ($x_i = 1$) or not ($x_i = 0$).

$$min \sum_{\forall i \in I} x_i \quad where\ x_i \in \{0,1\} \tag{1}$$

The constraints of equation (1) are presented next. It is to extract the best shooting position for each mesh: the SfM process requires that each mesh be shot from at least two viewpoints to measure the distance by triangulation.

P_{ji} indicates whether mesh P_j (the j -th polygon) is visible from viewpoint i, with $P_{ji} = 1$ denoting visibility and $P_{ji} = 0$ indicating invisibility. The index i corresponds to the aerial

viewpoint described above, and j refers to the polygon index. This visibility determination can account not only for occlusion caused by the back side of the target object but also for occlusion by other external objects. In such cases, the visibility condition for P_{ji} must be further refined. However, this paper does not consider such extensions and leaves them as future work.

$$subject\ to \sum_{\forall i \in I} P_{ji} x_i \geq r, \forall j \in J \tag{2}$$

In each mesh, the binocular parallax of approximately 30° is represented by $A = [A_1 \cdots A_j]$. A_j is the symmetric matrix, A_{jkm} is defined as 1 if the binocular parallax between camera K and camera m with respect to the center of gravity of mesh J is approximately 30°, and 0° otherwise. Equation (3) is used as the constraint condition.

$$subject\ to \sum_{\forall i \in I} A_{jni} x_i \geq (r-1), \forall j \in J, \forall n \in I \tag{3}$$

The photography point obtained by the above equations (1)-(3) is used as a reference for the drone's flight path.

An advantage of drones is their ability to change the direction of travel without changing the direction of the aircraft through sudden movements such as turning around or forced deceleration. Therefore, constant-speed flight can be achieved by setting a waypoint with an appropriate drone turn path. Two constraint conditions were set to enable this.

The first is the upper limit of the bank angle relative to the travel direction. Specifically, the distance from the drone to the destination and the steering angle ψ_{MAX} per fixed distance L of the drone are set. Thus, the maximum bank angle φ_{MAX} from the drone point to the destination is determined.

$$\varphi_{MAX} = \frac{L}{l} \cdot \psi_{MAX} \tag{4}$$

The second constraint is the turning radius R. The turning radius R can be derived from Equation (5). V is the speed of the drone, θ is the upper limit of the bank angle derived in Equation (4), 11.26 is the gravitational acceleration converted to feet value.

$$R = \frac{V^2}{11.26 \cdot \tan\theta} \tag{5}$$

Therefore, the trajectory of the drone was revealed if it turned at the maximum bank angle. The intersection of this trajectory and the vector from the current location to the destination are determined. Assuming that the distance to an intersection is less than or equal to the distance to the destination, the destination can be reached within the maximum bank angle and is used as the waypoint. If the distance to the intersection is greater than the distance to the destination, the destination cannot be reached even at the maximum bank angle. In this case, the waypoint is the intersection of the normal vector from the current location to the destination through the destination and the locus at the maximum bank angle.

The trajectories and waypoints calculated above were used to set the route. The starting and goal points must be updated to adapt to these conditions. In this study, the starting point was set at the location of the drone. The drone movement vector was determined by connecting the coordinates of the start and drone points before rotating 180 °around the starting point. The goal point was the point next to the optimal aerial photography point that the drone had been aiming for until then.

If the vector between the drone's current location and the next optimal aerial point is $\overrightarrow{a_i}$ and the inverse vector between the drone's current location and the previous waypoint is $\overrightarrow{b_i}$, Equations (6) and (7) represent the angle formed between and the optimal aerial photography point P_i.

$$\cos\theta = \frac{\overrightarrow{a_i} \cdot \overrightarrow{b_i}}{|\overrightarrow{a_i}||\overrightarrow{b_i}|} \tag{6}$$

$$P_i = \overrightarrow{a_i} \cdot \cos(\theta - \varphi_{MAX}) \tag{7}$$

Connecting the trajectories between the waypoints calculated in these manners creates a final route plan for the drone to fly without slowing.

These settings enabled the creation of a flight path that did not slow down the drone.

3.3 Calculation of Aerial Photography Points

This section presents the aerial photography points on the calculated route. The issue with photography from the waypoint calculated in the previous section is the distance from the utility poles compared to the optimal aerial photography point of Yamazaki et al. The accuracy of a 3D model depends on image resolution. Therefore, the farther the photography point is from the object, the less accurate the 3D model becomes. To address this issue, the algorithm proposed by Moritani et al. was used to calculate the optimal additional photography point. Specifically, additional photography was performed to ensure efficient photography without compromising the 3D model quality.

Moritani et al. used two indices to find additional photography points. The first is an evaluation index for orthogonal photography. The second factor is the evaluation index of the baseline ratio. The baseline ratio is the ratio of the distance between the two images to the distance from the image to the target. These two indices are used to calculate the optimal additional photography points.

The evaluation index for positive photographs was calculated using Equation (8), where c_i represents multiple representative points between the waypoints obtained in the previous section. In this study, ten points were set between each waypoint as candidates for c_i. p is the center of gravity of each mesh when the poles are meshed, and n is the average vector of the poles at the center of gravity of each mesh. Using the above variables, we obtained an evaluation index of directly opposite photographs from each representative point in the pathway to the center of gravity of each mesh.

$$NBV^i_{frontarity} = 1 - \left(n \cdot \frac{c_i - p}{\|c_i - p\|}\right) \tag{8}$$

The baseline ratio evaluation index was calculated as follows. BH^i indicates whether the angle formed by the additional photography point candidate c_i and reference image point P_r centered at the center of gravity P of each mesh is within the specified angle. This study sets it at 45 °,

which is the same value as the standard angle of view. Although the reference image points c_r initially corresponds to the optimal aerial photography point, there are cases where it does correspond via the optimal aerial photography point. In this case, the candidate's additional photography point, located at the nearest coordinate to the optimal aerial photography point, was used as the reference image point c_r . The intermediate value between c_r and c_i is c_{ri} . According to Moritani, the recommended angle between images is 20–30 °, and 0.536 is used as a representative value for the ratio between an object and two images. Therefore, this value was used in this study.

$$BH^i = \left| \frac{\|c_i - c_r\|}{\|c_{ri} - p\|} - 0.536 \right| \quad (9)$$

$$NBV_{BH}^i = \frac{BH^i - BH_{max}}{BH_{min} - BH_{max}} \quad (10)$$

The baseline ratio obtained in Equation (9) was used in Equations (8) and (10) to calculate the evaluation index for each additional photography point candidate c_i, where w is the weight. In this study, $w_f = w_{BH} = 1/2$ to use both evaluation indices equally, according to the method described by Moritani et al. From the above, the candidate additional photography point $c_i \in C$ with the lowest value is the optimal additional photography point c_{NBV}.

$$c_{NBV} = \underset{c_i \in C}{argmin}\left(w_f \cdot NBV_{frontarity}^i + w_{BH} \cdot NBV_{BH}^i\right) \quad (11)$$

4 EVALUATION SUMMARY

This study evaluated the compatibility between the temporal efficiency and 3D model accuracy. The accuracy of the 3D model was evaluated using the accuracy prediction index of the 3D model used by Moritani et al. Time efficiency involves the time required for aerial photography. In addition, the minimum photography point calculated using the optimal photography planning method of Yamazaki et al. was used for comparison. Yamazaki et al. assumed that the camera stops and shoots from the minimum photography point. In this evaluation, the aircraft is assumed to stop at the minimum photography point for a certain period and fly straight between the minimum photography points while accelerating and decelerating.

4.1 Parameter Settings

The poles evaluated in this study were 16-m high and 340-mm in diameter and were used as reference poles with a height of 16 m, terminal diameter of 240 mm, and former diameter of 453 mm. In this study, we evaluated the differences between the proposal and the conventional method before evaluating the attachments to the utility poles. Therefore, as a basic evaluation, we evaluated the differences between the proposal and the conventional method by evaluating the attachments and surrounding structures. In addition, the utility pole was divided into eight sections in the circumferential direction and eight in the vertical direction, totaling 64 voxels each. Therefore, the tie points were the vertices of each voxel, resulting in 72 candidate tie points.

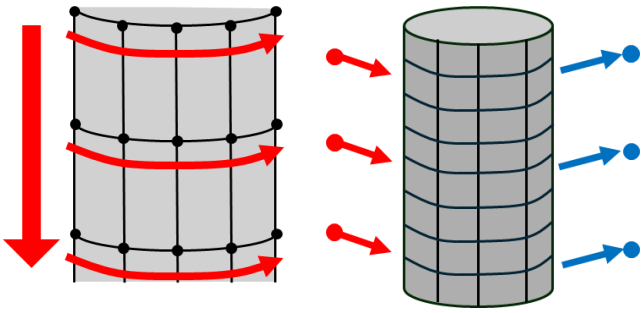

(a)Order of tie points (b) Potential starting and finishing points

Figure 3: Parameters of utility poles

The accuracies of the tie-point candidates were evaluated. The tie points were numbered from the top of the poles, as shown in Fig. 3(a). Based on the above conditions, the degree of shape degradation at all the tie points was evaluated using the conventional and proposed methods. The speed of the drone in this evaluation varied, but the acceleration was unified at 10 km/h/s. This value was determined because the maximum acceleration of a typical aircraft is approximately 10 km/h^2. The drone's candidate starting and finishing points are at the top and bottom of the utility poles, respectively, as shown in Fig. 3(b).

4.2 Method of Evaluating Accuracy

Moritani et al.'s method was used as the evaluation value to assess the accuracy. Moritani et al. used the following six indices. This evaluation method predicts the quality of a high-density model based on the tie points that constitute the vertices of the 3D model and the camera pose of the captured image.

① Reliability F_R (Fig. 4(a))
Evaluate the number of images with visible tie points.

$$F_R(i) = |V_i| \quad (12)$$

② Average of mesh area F_a (Fig.4(b))
The average surface mesh area $A_{i,n}$ of the n th approximate object connected to the tie point i on the surface of the approximate object is denoted by $F_a(i)$ and evaluated using Equation (13).

$$F_a(i) = \frac{1}{N_{A^i}} \cdot \sum_{n=0}^{N_{A^i}} A_n^i \quad (13)$$

③ Average of mesh edges F_e (Fig.4(c))
In the approximate object surface model, the edge lengths e^i connected to the tie point i are calculated, and their average value F_e is evaluated using Equation (14), where F_e is the number of edges connected to tie point i.

$$F_e = \frac{1}{N_{e^i}} \cdot \sum_{n=0}^{N_{e^i}} e_n^i \quad (14)$$

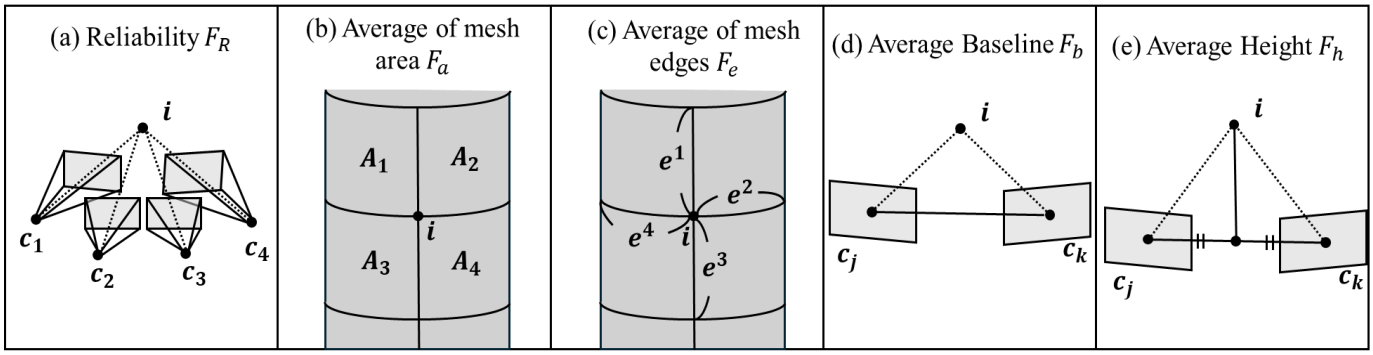

Figure 4: Summary chart of quality prediction indicators

④ Average Baseline F_b (Fig.4(d))

The distance between the centers of projection c_j and c_k of the two visible cameras j and j were calculated from the tie point i and evaluated using Equation (15), with F_b as the average value for all camera pairs.

$$F_b = \frac{1}{{}_{N_{ci}}C_2} \cdot \sum_{j=0}^{N_{ci}} \sum_{k=j+1}^{N_{ci}} \|c_j - c_k\| \quad (15)$$

⑤ Average Height F_h (Fig. 4(e))

The distance from point c_j, c_k, which bisects the baseline of two cameras j, j visible from tie point i, to tie point i was calculated and evaluated using Equation (16) with F_h as the average value for all camera pairs.

$$F_h = \frac{1}{{}_{N_{ci}}C_2} \cdot \sum_{j=0}^{N_{ci}} \sum_{k=j+1}^{N_{ci}} \|p_i - c'_{jk}\| \quad (16)$$

⑥ Base line ratio F_{bh}

The ratio of the average baseline length to the average subject distance at tie point i is F_{bh} and is evaluated using Equation (17).

$$F_{bh} = \frac{F_b(i)}{F_h(i)} \quad (17)$$

Each quality prediction index $F_X(i)(X \in R, a, e, bh)$ derived in Equations (12)-(17) is normalized using Equation (18) below and converted to $E_X(i)(\in [0,1])$.

$$E_X(i) = 1 - L \cdot (F_X - \mu_X, \sigma_X) \quad X \in [R, a, e, bh] \quad (18)$$

Here, μ_X is the mean of indicator $F_X(i)$, σ_X is the standard deviation, and $L(F_X - \mu_X, \sigma_X) = 1/(1 + \exp\left(\frac{-2(x-\mu)}{\sigma}\right))$ is the standard deviation.

$$E_{deg}(i) = \frac{E_R + E_a + E_e + E_{bh}}{4} \quad (19)$$

Finally, the average of the six energies $E_X(i)$ values was used to evaluate the degree of shape degradation, $E_{deg}(i)$, using Equation (19). $E_{deg}(i)$ has a value between 0 and 1. The higher the value, the greater the shape degradation and the less accurate the 3D model. Therefore, a value closer to 0 indicates higher accuracy of the 3D model.

4.3 Methods of Efficiency Evaluation

In this study, efficiency was evaluated based on the aerial photography time per utility pole. The procedure for calculating the specific aerial photography time varied depending on the method used. In the conventional method, the drone must stop at each photography point; therefore, acceleration and deceleration are performed between each photography point based on the acceleration of the drone. Thus, the aerial photography time between each photography point in the conventional method is $t = 2 \times \sqrt{L/a}$, where a is the acceleration.

By contrast, the proposed method requires an aircraft to fly at a constant speed of v without decelerating. Therefore, the photography time t between each photography point in the proposed method was $t = L/v$.

5 EVALUATION RESULT

5.1 Evaluation Per Utility Pole

5.1.1 Comparison Between Previous and Proposed Methods

In this section, I present the results of a comparison and evaluation of the proposed method with the conventional aerial photography method after hovering. I used a multirotor drone to perform the comparison and verification to make the two methods compatible. I compared the flight times for the shape degradation degree and speed at each tie point.

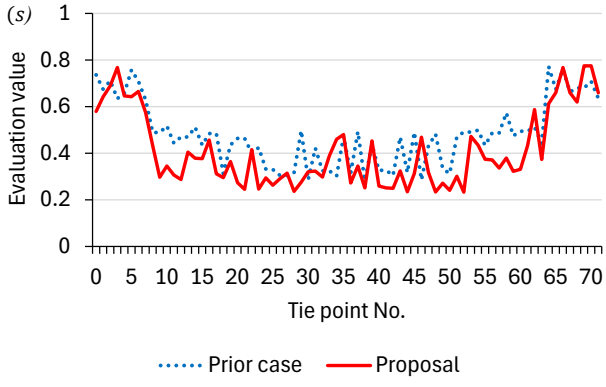

Figure 5: 3D model prediction accuracy for each tie point

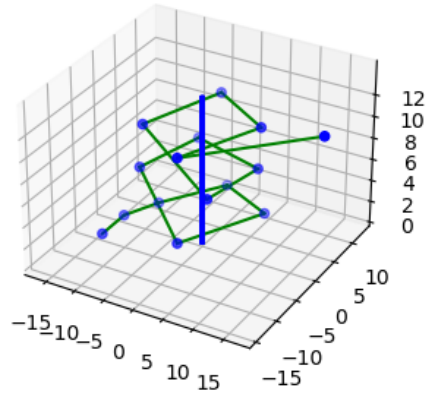

(a)

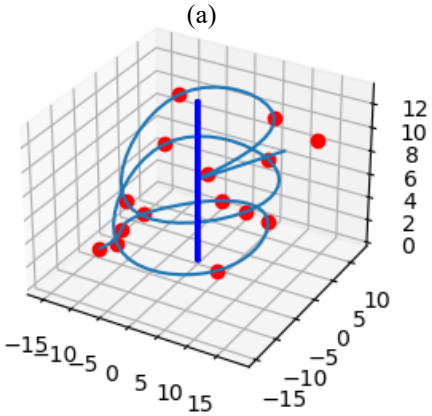

(b)

Figure 6: Comparative chart of flight routes

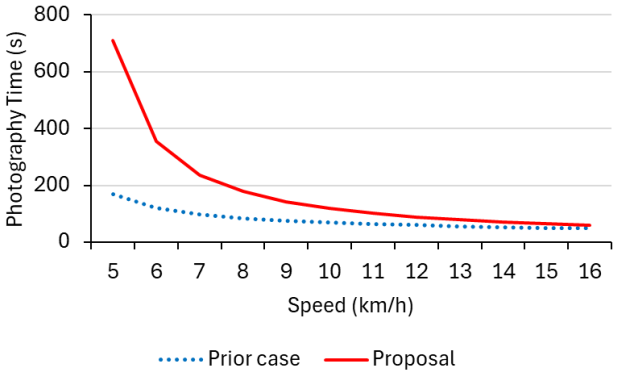

Figure 7: Relationship between speed and efficiency

As a result of the accuracy evaluation, the degree of shape degradation at each tie point is shown in Fig. 5. The average value of the shape degradation for the conventional method was 0.48, and the average value of the shape degradation for the proposed method was 0.41; thus, the shape degradation was improved by 0.07, but this was not a significant difference.

Next, the results of the efficiency evaluation are presented. The path of the proposed method using a multirotor drone is illustrated in Fig. 6(a), and the path for the conventional method is shown in Fig. 6(b). In addition, Fig. 7 shows a graph of the relationship between the upper limit of speed and aerial photography time. In the conventional method, the acceleration was set to 10 km/h; however, because the distance between the ideal photography points was not very

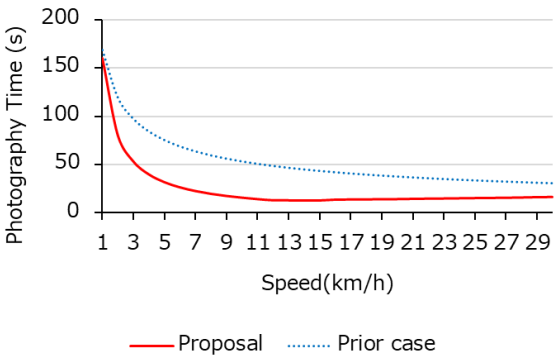

Figure 8: Speed impacts from the multirotor-type and the VTOL-type

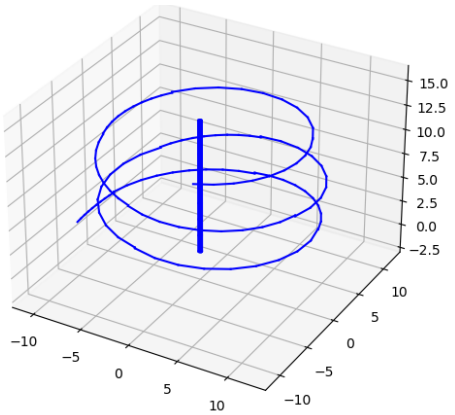

(a)

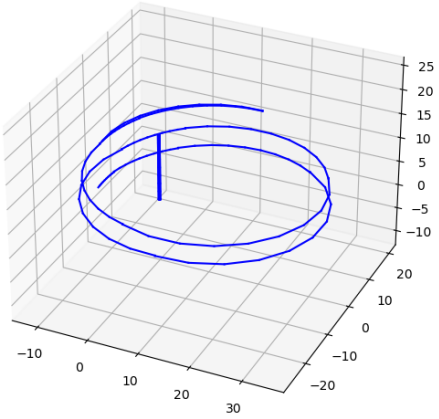

(b)

Figure 9: 10km/h flight path and 15km/h flight path

long and was also constant, even if the upper limit of speed was increased, there was no significant impact on the aerial photography time. On the other hand, in the proposed method using a multirotor drone, the total length of the route does not change significantly even if the speed changes owing to the calculation method of the route. Therefore, as the speed increased, aerial photography time decreased. This indicates that multirotor drones can turn on a dime. In both methods, it was found that as the speed increased, the characteristics of the multirotor drones Ire reflected, and the aerial photography time converged to a similar value.

From the above, I can conclude that this algorithm is valid because there was no significant difference in either the 3D

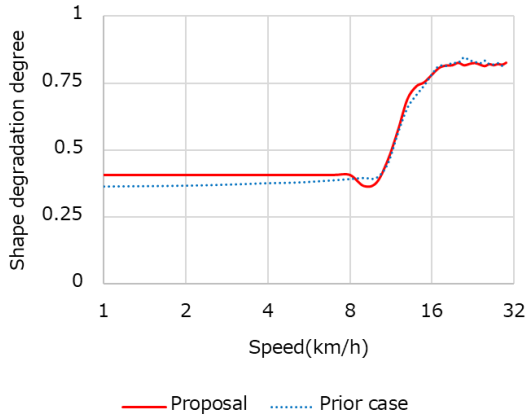

Figure 10: Relationship between speed and evaluation value

model accuracy or efficiency evaluation when the type of drone used was unified.

5.1.2 Comparison of VTOL and Multirotor Drones

In this section, we evaluate the suitability of the proposed method using VTOL-type and multirotor-type drones for aerial photography in terms of both accuracy and efficiency and describe the results of the comparison.

First, we present the results of efficiency evaluation. Figure 8 shows the relationship between the speed and total aerial photography time. The VTOL-type drone captured photographs in a shorter time than the multirotor-type drone. When the upper limit is set at 10 km/h, the result is that the VTOL type can complete filming in 27.4% of the time taken by the conventional method. However, as the upper limit of the speed increased, the difference became smaller. This was because the total distance of the aerial filming route increased as the speed increased. In addition, as a characteristic of the aerial filming route, up to a speed of approximately 12 km/h, the aerial filming route followed a circular path around the utility poles at equal intervals, as shown in Fig. 9(a). However, when it exceeds that, the aerial photography route becomes one that passes close to the utility pole on one side but traces a route that is away from the utility pole on the other side, as shown in Fig. 9(b).

Next, we examined the accuracy evaluation. Figure 10 shows the relationship between the maximum speed and average shape degradation value. The graph indicates that there was no significant variation in accuracy. This is because the aerial photography route for both the VTOL drones and multirotor drones draws a large arc as the speed increases. The farther away from the utility pole, the lower the 3D model accuracy, which is why we obtained this result.

Summarizing the above results on the temporal efficiency and 3D model accuracy, the VTOL drone showed the highest efficiency at 12 km/h. In the 3D model accuracy evaluation, the VTOL drone showed the highest accuracy at 10 km/h, although there was no significant difference from that of the multirotor drone.

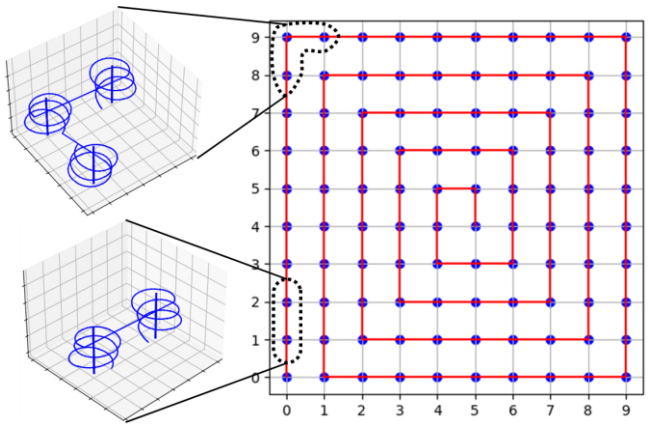

Figure 11: Manhattan model with 100 utility poles

Therefore, it was determined that using a VTOL drone at a speed of 10 km/h was the most suitable for achieving both efficiency and accuracy.

5.2 Evaluation Per 100 Utility Poles

To date, evaluations have been based on a single utility pole. We expanded the evaluation to 100 utility poles and calculated the number of drones and how long it would take to inspect all utility poles in Japan. In this verification, we calculated the pattern of VTOL drones using the proposed method, which can achieve both temporal efficiency and 3D model accuracy. The route was calculated as a Manhattan model with 100 utility poles at 40m intervals, for a total of 100, and the time for aerial photography was calculated. The speed was set at 10 km/h. In this verification, the route connecting the utility poles is set such that the angle formed by the final point of each utility pole, the route between the utility poles, and the starting point of the next utility pole are obtuse. This was added as a constraint such that the drone could fly without having to tilt the aircraft excessively. In addition, the starting point of the Manhattan model was set as the utility pole located at the corner. However, a goal was not set. This is because it is possible to set a more flexible path.

The aerial photography route in the Manhattan model is shown on Fig. 11. From the evaluation results, it can be seen that the common points of the straight and corner sections of the route are that the aerial photography route is upside-down and lined up alternately. From the results of the above verification using the Manhattan model, the total distance of the route for photographing 100 utility poles was approximately 21.7 km, and the total times for photographing them at 10 km/h were 36 min and 7 s, respectively. If one drone is operated for six hours per day, it is possible to inspect approximately 1,000 utility poles. If 100 VTOL drones are in operation, it is estimated that 35.78 million utility poles can be inspected in one year.

6 CONCLUSION

In this paper, we propose and verify a method for efficiently generating flight paths for aerial photography using drones, with the aim of reducing the labor required for inspecting utility poles in Japan. Utility poles are a critical infrastructure

supporting power and telecommunications networks; however, due to their large number and wide distribution, they are currently inspected manually. To carry out 3D model inspections of utility poles using drones, which are used for bridges and dams, it is necessary to plan the flight path and aerial photography points so that many utility poles can be photographed efficiently in a single flight.

Therefore, we devised an algorithm that aims to pass through the theoretically optimal photography position of the utility pole and searches for the optimal photography point on the main flight route while prioritizing constant-speed flight, thereby improving the model generation accuracy. Through computer evaluation, we confirmed that, compared to previous studies that assumed multirotor drones, the model accuracy of VTOL drones and this algorithm is equivalent, but flight time can be reduced by 72.6%.

Utility poles are normally accompanied by things like electrical wires, but this study only carried out a basic evaluation, so it did not take this into account. Therefore, it should be noted that this study assumes a single cylindrical object that mimics a utility pole. Future work should include evaluations with added accessories and aim to advance closer to actual field verification. On a similar note, this study did not consider the gimbal of the camera since only a basic evaluation was conducted. Since the gimbal is related to the internal factors of the camera, evaluating this can bring us closer to a demonstration experiment.

Also, although there are buildings and other structures around utility poles, this study only conducted a basic evaluation and did not take this into account. Therefore, it should be noted that the environment was ideal with no obstacles around the poles. This is one of the external factors that affect the evaluation environment. There are also other external factors related to optics, such as shadows from the utility poles themselves. Future research should focus on a more detailed subdivision of the external factors. It is necessary to evaluate each factor and approach the actual field verification. By conducting field evaluations that include these factors, it is possible to verify their practical use.

REFERENCES

[1] J. R. Gibson, “Built to Last Challenges and Opportunities for Climate-Smart Infrastructure in California”, Union of Concerned Scientists, pp.6 (2017).

[2] The WHITE HOUSE, “Fact Sheet: The President’s Plan to Make America a Magnet for Jobs by Investing in Manufacturing”, https://obamawhitehouse.archives.gov/the-press-office/2013/02/13/fact-sheet-president-s-plan-make-america-magnet-jobs-investing-manufactu (2013).

[3] U. S. Department of Transportation Federal Highway A dministration, “Highway History, In Memory of Ronal d Reagan”, https://www.fhwa.dot.gov/infrastructure/reagan.cfm (2017).

[4] Ministry of Land, Infrastructure, Transport and Tourism, “Changes in Utility Pole Phoenixes”, https://www.mlit.go.jp/road/road/traffic/chicyuka/chi_13_03.html (2024).

[5] Z. Tian, L. Jianhua, “A 3D Reconstruction Method for Pipeline Inspection based on Multi-vision”, Measurement, Vol.98, No.5, pp.35-48 (2017).

[6] H. Miyake, M. Fujiu, S. Nakayama, J. Takayama, “Evaluation of Infrastructure Conditions by 3D Model Using Drone”, 4th International Conference on Road and Rail Infrastructure, Vol.9, No.3, pp.597-602 (2016).

[7] Ministry of Land, Infrastructure, Transport and Tourism, “Securing Infrastructure Development Leaders, Improving On-Site Productivity, Introducing New Technologies, etc.”, https://www.mlit.go.jp/hakusyo/mlit/h27/hakusho/h28/html/n1321000.html(2024).

[8] T. Ishida, K. Nakata, J. Okui, S. Yamada, “Verification of a method for surveying river basins using VTOL drones in emergency situations (in Japanese)”, Proceedings of the 2024 Japan Society of Erosion Control Research Meeting, No.19, pp. 323-324 (2024).

[9] D. Kubo, “History and Technological Development of Unmanned Aircraft Systems (Drones) (in Japanese)”, Measurement and Control: journal of the Society of Instrument and Control Engineers, Vol.56, No.1, p.12-17(2017).

[10] J. B. Sankey, S. Ravi, C. S. A. Wallace, R. H. Webb, T. E. Huxman, “Quantifying Soil Surface Change in Degraded Drylands: Shrub Encroachment and Effects of Fire and Vegetation Removal in a Desert Grassland”, Journal of Geophysical Research: Bio geosciences: Vol.117, Issue G2(2012).

[11] D. Moon, S. Chung, S. Kwon, J. Seo, J. Shin, “Comparison and Utilization of Point Cloud Generated from Photogrammetry and Laser Scanning: 3D world model for smart heavy equipment planning”, Automation in Construction, Vol.98, Pages 322-331(2019).

[12] S. Yoon, G. Gwon, J. Lee, H. Jung, “Three-Dimensional Image Coordinate-Based Missing ROI Area Detection and Damage Localization for Bridge Visual Inspection Using Unmanned Aerial Vehicles”, Structural Health Monitoring, Vol.20, No.4, pp.1462-1475 (2020).

[13] R. Moritani, S. Kanai, H. Date, Y. Niina, R. Honma, “View Planning for High-quality and Efficient as-is Model Reconstruction by SfM-MVS (6th report) ― Estimation of the Additional Camera Poses Based on The Extracted Low-Quality Regions ―(in Japanese)”, 2020 Journal of the Japan Society of Precision Engineering, No.22, pp.43-44 (2020).

[14] K. Yamazaki, K. Okahara, A. Minesawa, “Proposal of an Optimal Imaging Planning Method for 3D Reconstruction Using Geospatial Information (in Japanese)”, IPSJ Symposium series DICOMO Multimedia, Distributed, Cooperative, and Mobile Symposium, (DICOMO 2023), pp.611- 616 (2023).

[15] H. Dan, N. Inazu, T. Ozaki, S. Kubota, and Y. Yasumuro, “Optiminal ff UAV Path Planning for Aerial Photography Survey of Outdoor Structures”, Japanese Journal of JSCE F3, Vol.74, No.2, pp.159-166 (2020).

Koji Yamagishi graduated from the Faculty of Information Frontier, Kanazawa Institute of Technology. He then entered the Graduate School of Engineering at Kanazawa Institute of Technology. He is a member of the Information Processing Society of Japan.

Yuichi Tokunaga received a Ph.D. degree in science and engineering from Ritsumeikan University in 2009. He joined Mitsubishi Electric Corporation in 1990 and engaged in R&D of the high-reliability computer, wireless sensor network, the algorithms of time-synchronization and pointing, the network protocol for industrial applications, and data analytics for CBM (Condition Based Maintenance). He has been a professor at Kanazawa Institute of Technology since 2019. He is a member of the ITS steering committee of IPSJ and a member of IEEE and ISCIE.